JOC The Journal of Organic Chemistry

pubs.acs.org/joc Article

Synthesis of Geminal Dibromovinyl Asymmetrically Modified Nonfullerene Acceptors and Their Photovoltaic Properties

Published as part of The Journal of Organic Chemistry special issue "Celebrating Nankai University's Legacy of Excellence in Organic Chemistry".

Jie Wang, Jingyi Huo, Xin Chen, Jinyi Yang, Longyu Li, Ruibin Bian, Wendi Shi, Zhaoyang Yao, Chenxi Li, Xiangjian Wan,* and Yongsheng Chen*

Cite This: J. Org. Chem. 2026, 91, 994−1003 Read Online

ACCESS | Metrics & More | Article Recommendations | Supporting Information

ABSTRACT: A nonfullerene acceptor (NFA), ACHV, is designed and synthesized by introducing a novel 2,2-dibromovinyl substituent onto the central quinoxaline unit. Compared with the control acceptor ACHM, the 2,2-dibromovinyl group profoundly modulates the electrostatic potential distribution, dipole moment, light-harvesting characteristics, and aggregation behavior of the acceptor ACHV. Consequently, organic solar cells (OSCs) based on ACHV achieve a power conversion efficiency (PCE) of 17.43% with simultaneously enhanced V_{oc} and FF without sacrificing J_{sc}. This work highlights a potential molecular design strategy for efficient OSCs.

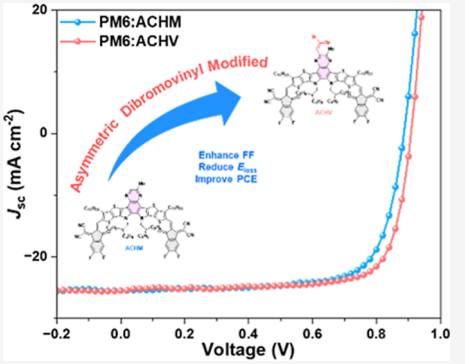

1. INTRODUCTION

In recent years, the advent of nonfullerene acceptors (NFAs), represented by ITIC and Y6, has remarkably boosted the device performance of organic solar cells (OSCs).[1−5] However, compared with inorganic and perovskite solar cells, OSCs still exhibit relatively low open-circuit voltages (V_{oc}), which mainly originates from substantial energy loss (E_{loss}). This E_{loss} predominantly stems from nonradiative energy loss (ΔE_{nr}), which mainly arises from charge recombination processes wherein excited electrons and holes recombine without the emission of photons.[6] To address this issue, several molecular and morphological strategies have been proposed: (i) regulating molecular polarizability to lower the exciton binding energy (E_b), thereby weakening vibrational coupling and reducing the driving force required for exciton dissociation;[7] (ii) suppressing energetic disorder via rational molecular design and morphology optimization to improve charge transport and mitigate defect-induced recombination;[8] and (iii) weakening electrostatic potential-induced intermolecular interactions to reduce the contribution of spin-forbidden processes and interfacial traps to nonradiative recombination, thereby enhancing V_{oc}.[9] Despite these advances, the simultaneous realization of reduced E_{loss} and optimized active-layer morphology, while increasing V_{oc} without compromising the short-circuit current density (J_{sc}) and fill factor (FF), remains a pressing challenge, which continues to limit the enhancement of OSC efficiencies.

In this context, asymmetric acceptor design provides an effective route for further mitigating energy loss in OSCs. By deliberately breaking molecular symmetry, intra- and intermolecular interactions can be precisely regulated, thereby tuning the photophysical properties, electrochemical behavior, and aggregated structures to support performance enhancement. Key strategies include (i) asymmetric side-chain engineering, (ii) asymmetric modification of the conjugated core, and (iii) the asymmetric design of electron-deficient end groups. Symmetry breaking induces permanent molecular dipoles that strengthen intermolecular packing and $\pi-\pi$ stacking, optimize donor−acceptor blend morphology, and construct efficient bicontinuous charge-transport networks. Meanwhile, asymmetric design enables fine control of frontier orbital energies and light-harvesting ranges, achieving synergistic optimization of multiple parameters and boosting PCE.[10−13] In addition, ternary strategies can further expand the device optimization room and boost the V_{oc} and PCEs of OSCs.[14,15]

Received: September 22, 2025
Revised: December 6, 2025
Accepted: December 18, 2025
Published: January 2, 2026

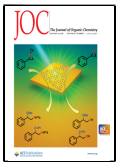

https://doi.org/10.1021/acs.joc.5c02377
J. Org. Chem. 2026, 91, 994−1003

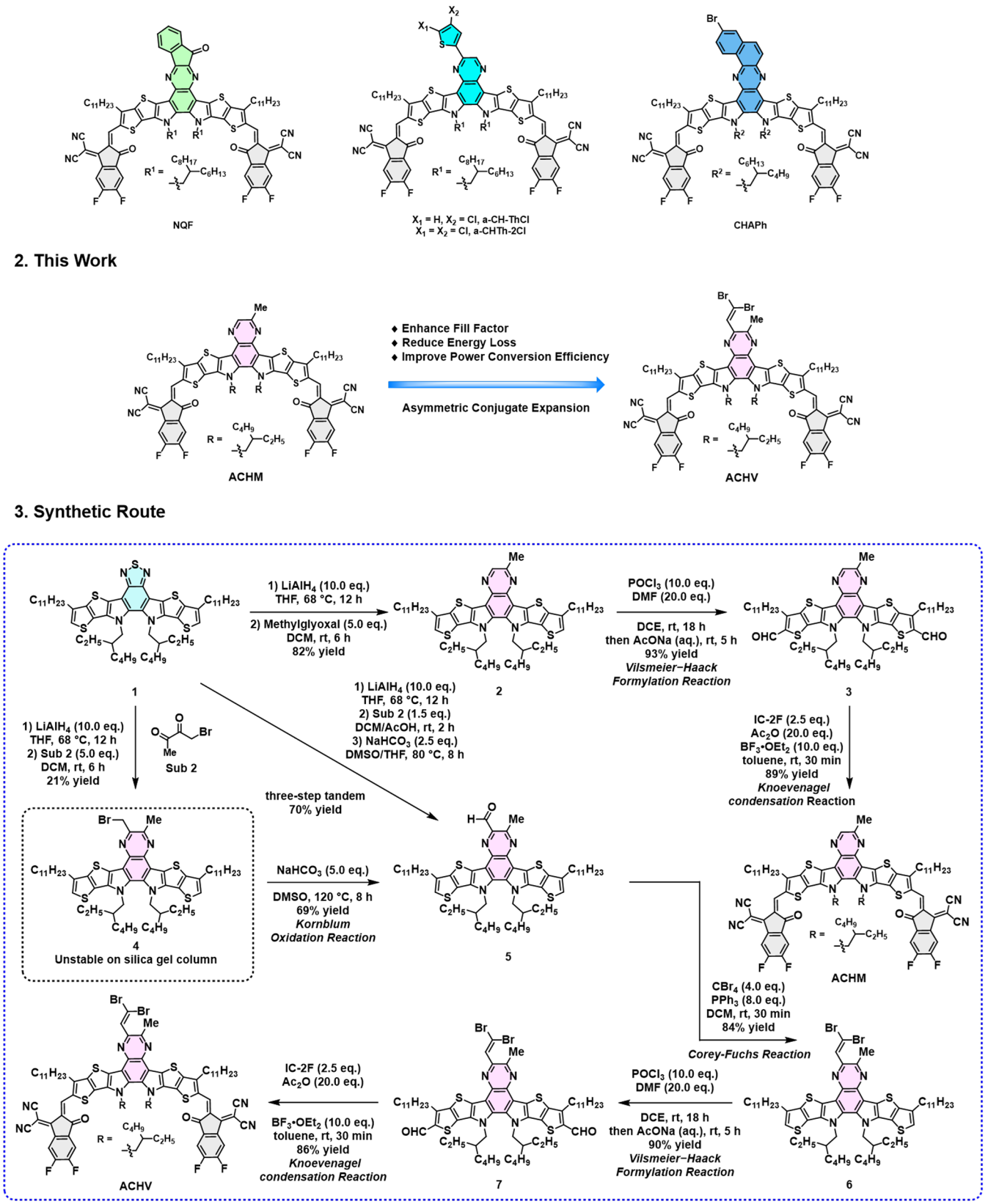

Figure 1. (a) Chemical structures of NQF, a-CHTh-2Cl, and CHAPh. (b) Chemical structures of ACHM and ACHV and their molecular design rationale. (c) The corresponding synthetic routes for ACHM and ACHV.

Our group reported a "central-unit asymmetric extension" strategy to develop new NFAs, aiming to provide a feasible approach for simultaneously reducing E_{loss} and optimizing active-layer morphology in 2022.[16] We first introduced an

https://doi.org/10.1021/acs.joc.5c02377
J. Org. Chem. 2026, 91, 994−1003

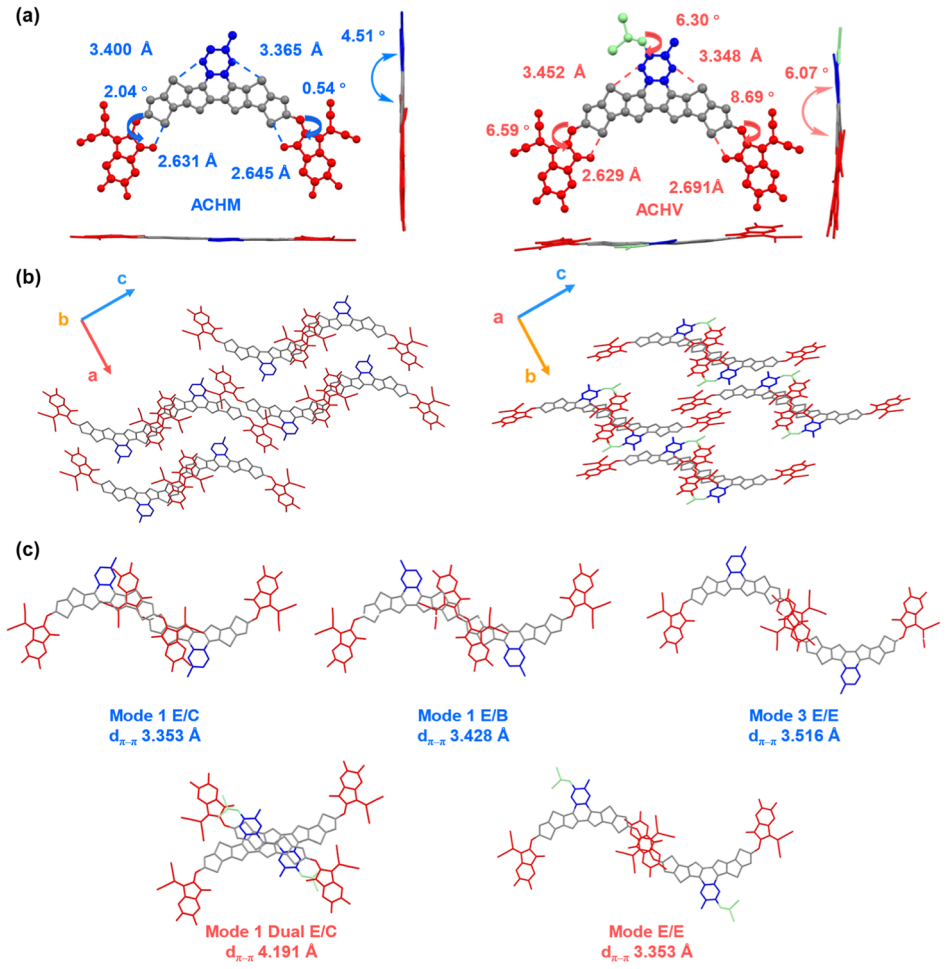

Figure 2. NFAs crystal structures. (a) Molecular structures of ACHM and ACHV. (b) Crystal packing topological structures from top view. (c) Main intermolecular packing modes with intermolecular potential over 70 kJ mol^{-1}. Note that the alkyl substitutions on SMAs were omitted for a clearer presentation.

indanone moiety into the central unit of a Y-series acceptor, successfully synthesizing an asymmetrically extended NFA (named NQF, Figure 1a), which exhibited a significantly reduced ΔE_{nr}. Subsequently, we further realized this design concept by constructing two NFAs, namely, a-CH-Th2Cl and CHAPh, through single-bond connection and fused-ring extension strategies, respectively. Two NFAs demonstrated suppressed ΔE_{nr} and enhanced PCEs, thereby validating the effectiveness of the asymmetric central-unit extension approach.[17,18]

In this study, 2,2-dibromovinyl ($Br_2C{=}CH-$) was selected as a novel asymmetric modification unit and incorporated into the central core of the ACHM (Figure 1b). The advantages of this substituent arise from the unique structural and electronic features of bromine; i.e., its high electronegativity imparts a strong electron-withdrawing inductive effect; the relatively large atomic radius (114 pm) with a diffuse outer electron cloud enhances π-conjugation and enables weak halogen bonding interactions;[19,20] and its steric configuration provides appropriate spatial hindrance. Experimental results reveal that 2,2-dibromovinyl significantly regulates the intrinsic molecular properties including electrostatic potential distribution, dipole moment, light-harvesting ability, and aggregation behavior, thereby optimizing blend morphology and improving photovoltaic performance. Compared with the unmodified ACHM, the ACHV not only effectively reduces E_{loss} and improves the V_{oc} but also enhances the FF owing to bromine-mediated optimization of molecular aggregation. As a result, the OSC based on ACHV achieves an impressive PCE of 17.43% with a V_{oc} of 0.908 V, a J_{sc} of 25.57 mA·cm^{-2}, and an FF of 75.40%. In contrast, the ACHM-based device demonstrates a PCE of 16.38% with a lower V_{oc} of 0.886 V, a lower J_{sc} of 25.46 mA·cm^{-2}, and an FF of 72.67%.

2. RESULTS AND DISCUSSION

To efficiently introduce the 2,2-dibromovinyl into the quinoxaline unit, quinoxaline intermediate 4 featuring a benzyl bromide structure was designed in this study. Due to its unique reactivity, this intermediate can be further converted into various functional groups, laying a foundation for subsequent modification. The detailed synthetic route is illustrated in Figure 1c. Starting from commercially available compound 1, a diamine intermediate was obtained via reduction with lithium aluminum hydride ($LiAlH_4$) following a method previously developed by our group.[21] This diamine intermediate was then subjected to in situ condensation with 1-bromo-2,3-butanedione, affording intermediate 4. Although thin-layer chromatography (TLC) monitoring indicated a high reaction yield, the actual yield of intermediate 4 was only 21% after column chromatography purification. Subsequent experimental verification revealed that intermediate 4 exhibits high sensitivity to

https://doi.org/10.1021/acs.joc.5c02377
J. Org. Chem. 2026, 91, 994−1003

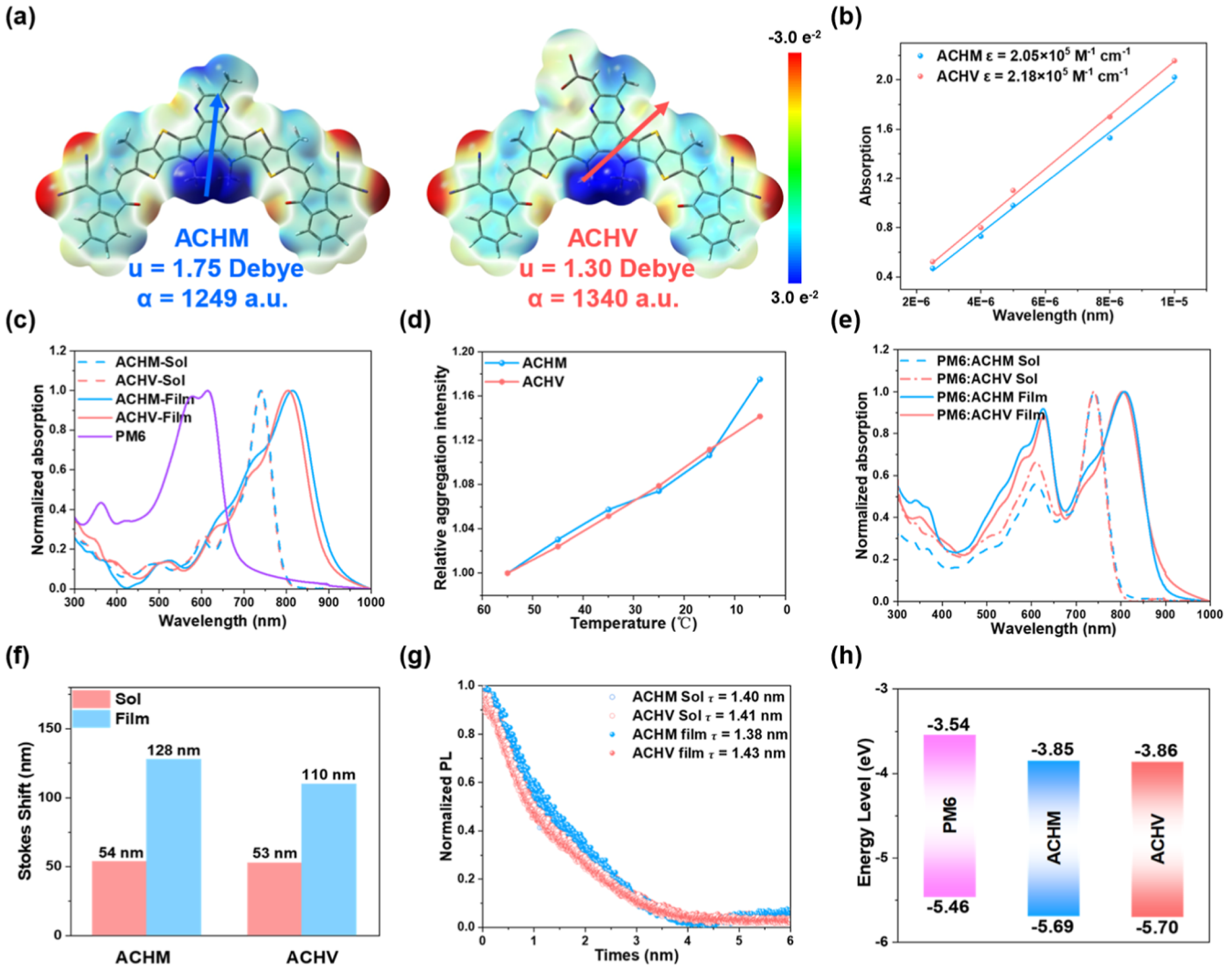

Figure 3. (a) DFT-calculated electrostatic potential (ESP) distribution, dipole moment, and polarizability of ACHM and ACHV. (b) Molar extinction coefficient of ACHM and ACHV. (c) Normalized absorption spectra of ACHM and ACHV in solutions and neat films. (d) Curves of ACHM and ACHV relative aggregation strength as a function of $CHCl_3$ solution temperature. (e) UV absorption of ACHM, ACHV, and PM6 in the $CHCl_3$ solution and blend films. (f) Stokes shifts for ACHM and ACHV in solution and neat films. (g) Time-resolved photoluminescence (PL) decay traces of ACHM and ACHM in solutions and neat films. (h) Energy level diagram of ACHM and ACHV.

silica gel and decomposes during column chromatography, which is the primary reason for its low yield. To address this issue, a one-pot synthesis strategy was adopted in this study: immediately after the in situ formation of intermediate 4, the solvent was removed via rotary evaporation without further purification. The crude product was directly subjected to the Kornblum oxidation reaction, enabling efficient conversion to quinoxaline formylated intermediate 5. After a simple optimization of reaction conditions, intermediate 5 was synthesized from compound 1 via a three-step, one-pot reaction, affording a yield of 70%. Following the acquisition of a sufficient amount of intermediate 5, its aldehyde group was efficiently converted to the 2,2-dibromovinyl via the Corey–Fuchs reaction, successfully synthesizing target central core 6. Finally, the target acceptor molecule ACHV was completed by combining the well-established Vilsmeier–Haack formylation reaction and the Knoevenagel condensation reaction. In summary, this work developed an efficient synthetic method: starting from commercially available compound 1, an asymmetric conjugated extended acceptor with a 2,2-dibromovinyl in the central unit was synthesized via 4 steps, with an overall yield of 45%. This method not only provides a feasible strategy for the asymmetric vinyl extension of the acceptor's central unit but also offers a new route for the functional group modification of quinoxaline-based materials.

As shown in Figure 2a, during the structural evolution from ACHM to ACHV, the combined effects of the steric hindrance effect and electron-withdrawing inductive effect of 2,2-dibromoethenyl result in significant torsion of the ACHV molecular backbone compared to ACHM. Driven by the steric hindrance effect of 2,2-dibromoethenyl, the dihedral angle between the central quinoxaline unit and the molecular backbone of ACHV reaches 6.07° (4.51° for ACHM); its electron-withdrawing inductive effect is directionally transmitted along the molecular backbone to the end groups, increasing the angles between the two end groups and the backbone of ACHV from 2.04° and 0.54° (for ACHM) to 6.59° and 8.69°, respectively.[22] Additionally, the distance of the S···O noncovalent interaction between the thiophene and end groups within the molecular backbone is slightly increased. Figure 2b shows the crystal packing structures of the two NFAs. Due to the identical molecular backbones of ACHM

https://doi.org/10.1021/acs.joc.5c02377
J. Org. Chem. 2026, 91, 994–1003

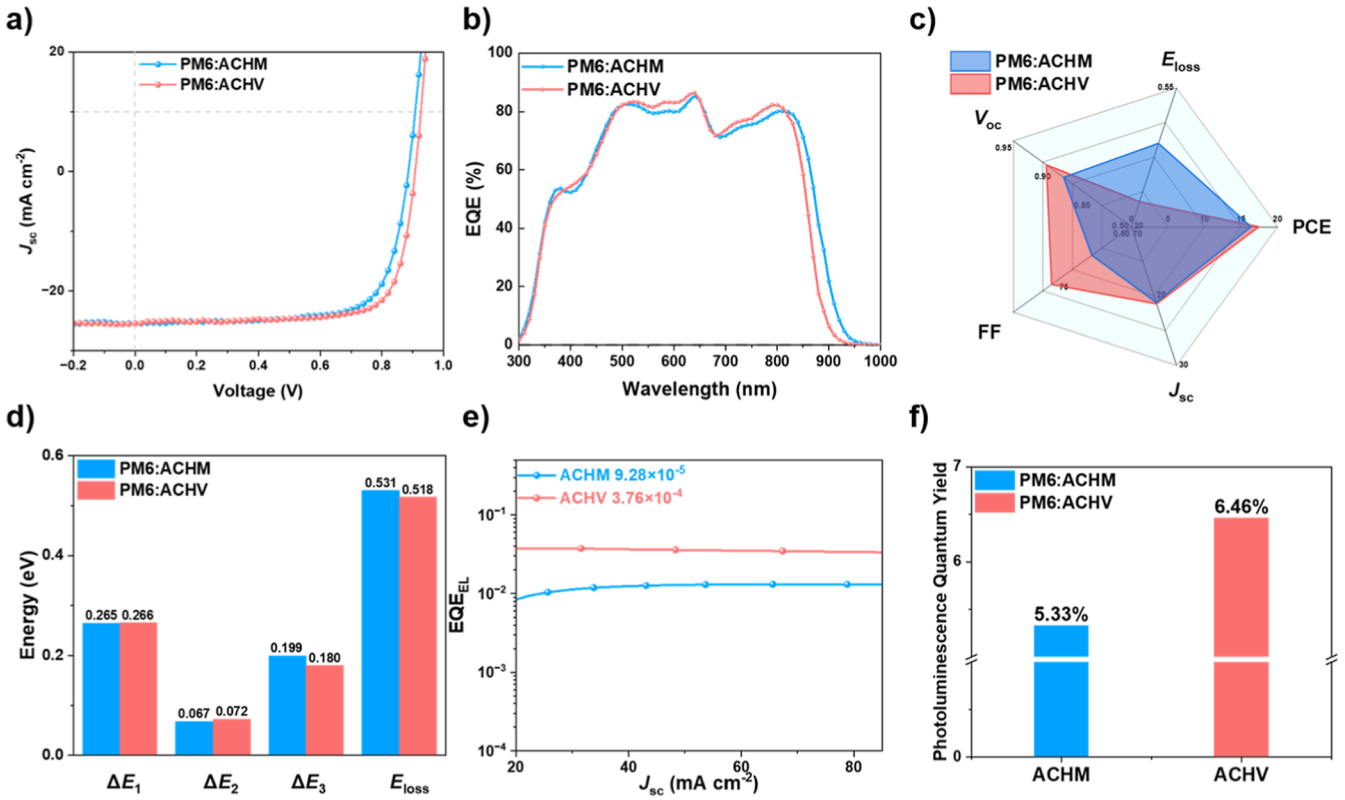

Figure 4. (a,b) $J-V$ and EQE curve for the optimized devices. (c) Parameter comparison for the binary OSCs. (d, e) E_{loss} and EQE$_{EL}$ diagram spectra for the optimized devices. (f) PLQY diagram spectra for ACHM and ACHV.

and ACHV, both form similar two-dimensional (2D) packing. However, significantly affected by the steric effect of 2,2-dibromoethenyl, the packing of ACHV is looser than that of ACHM. As presented in Figure 2c, ACHM exhibits three characteristic packing modes, end-to-center (E/C), end-to-backbone (E/B), and end-to-end (E/E), with corresponding packing distances of 3.353, 3.428, and 3.516 Å, respectively. In contrast, ACHV only displays two packing modes, dual end-to-center (Dual E/C) and end-to-end (E/E). Notably, the packing distance of the Dual E/C mode in ACHV increases significantly to 4.191 Å (much larger than the 3.353 Å of the E/C mode in ACHM), while the packing distance of its E/E mode decreases to 3.353 Å (slightly lower than the 3.516 Å of the E/E mode in ACHM). The above results indicate that 2,2-dibromoethenyl can precisely regulate the molecular packing structure through the synergistic control of steric effects and electronic effects.

To investigate the regulatory effect of asymmetric 2,2-dibromovinyl modification at the central unit on the molecular structure, density functional theory (DFT) calculations optimized the single-molecule geometries and electrostatic potential (ESP) surfaces of the two SMAs. Figure 3a shows that the dipole of the ACHV moment decreases significantly compared with that of ACHM after postmodification, indicating weakened intramolecular charge separation. The increased polarizability reflects the effective conjugation extension by 2,2-dibromovinyl, which enhances light-harvesting and external electric field interaction. The expanded conjugation improves electron cloud deformability, promoting photon-induced electron dynamics and optimizing aggregated-state charge separation/transport via intermolecular electron cloud coupling. ESP analysis further reveals that the 2,2-dibromovinyl introduces localized negative charges near the modification site, thereby reshaping the overall electrostatic distribution of the molecule. This change in electrostatic distribution induces specific noncovalent interactions, which guide the ordered assembly of molecules in the aggregated state and favor the formation of active layer morphologies that enable efficient exciton dissociation and charge transport.

Optical property measurements, as shown in Figure 3b, reveal that the molar extinction coefficient (ε) of ACHV is higher than that of ACHM, with values of 2.18×10^5 M^{-1} cm^{-1} and 2.05×10^5 M^{-1} cm^{-1}, respectively. This is attributed to the conjugated extension ability of the 2,2-dibromovinyl unit. It not only extends the intramolecular π-conjugated system of ACHV s but also enables the p-orbitals of bromine atoms to form p-π conjugations with the π-conjugated system, further promoting electron delocalization. This increases the probability of intramolecular electron transitions, ultimately leading to an enhancement in ε. Notably, as shown in Figure 3c, the maximum absorption wavelengths (λ_{max}) of ACHM and ACHV in solution are nearly identical, at 739 and 740 nm, respectively. However, their λ_{max} values in the thin-film state exhibit a significant difference, with the ACHM at 817 nm and the ACHV at 804 nm. The absorption properties of molecules in the thin-film state are dominated by intermolecular packing behavior.[23] The steric hindrance of the 2,2-dibromovinyl unit outside the quinoxaline ring in ACHV hinders the close contact between the conjugated planes of adjacent molecules, leading to the slight blueshift in the film absorption compared to ACHM. Quantitative analysis of the aggregation behavior (Figure 3d) confirms that both the relative aggregation intensity (RAI) and aggregation rate of ACHM are higher than those of ACHV, with ACHV exhibiting weaker

https://doi.org/10.1021/acs.joc.5c02377
J. Org. Chem. 2026, 91, 994−1003

Table 1. Photovoltaic Parameters of the Optimized Binary Devices[a]

devices	V_{oc} [V]	J_{sc} [mA cm^{-2}]	FF [%]	J_{sc}^{cal}[a] [mA cm^{-2}][b]	PCE [%]
ACHM	0.886 (0.884 ± 0.002)	25.46 (25.14 ± 0.28)	72.67 (73.03 ± 0.30)	24.76	16.38 (16.23 ± 0.15)
ACHV	0.908 (0.092 ± 0.004)	25.57 (25.57 ± 0.42)	75.40 (74.63 ± 0.84)	24.18	17.43 (17.21 ± 0.11)

[a]Average parameters calculated from 8 independent OSCs. [b]Current densities are calculated from EQE curves.

temperature dependence. This characteristic is beneficial for reducing the temperature sensitivity of molecular packing modes during solution processing.[24] Interestingly, as shown in Figure 3e, when ACHM and ACHV are each blended with the donor PM6, the differences in their λ_{max} values are negligible. This phenomenon may be attributed to the regulatory effect of the 2,2-dibromovinyl unit on the aggregation behavior of the acceptors being overshadowed by the D/A interactions, thereby leading to a reduction in the differences in maximum absorption peaks and cutoff absorptions between the two acceptors in the blended films.

Consistent with their UV absorption characteristics, both the Stokes shift ($\Delta\lambda_{stoke}$) and exciton lifetime (τ) of ACHM and ACHV display pronounced dependence on the aggregation state. As shown in Figure 3f−g, in dilute chloroform solutions, their $\Delta\lambda_{stoke}$ values are nearly identical (54 nm for ACHM and 53 nm for ACHV), and their τ values are also comparable (1.40 ns for ACHM and 1.41 ns for ACHV). This similarity can be attributed to the fact that solvent molecules in dilute media suppress intermolecular interactions, thereby making intramolecular vibrational relaxation the dominant excited-state decay pathway. In contrast, in the thin-film state, the two compounds exhibit markedly different optical behaviors. For $\Delta\lambda_{stoke}$, ACHM, which lacks bulky substituents, tends to form dense $\pi-\pi$ stacking, thereby enhancing nonradiative relaxation and increasing its $\Delta\lambda$ stoke to 128 nm, compared with 110 nm for ACHV.[25] Regarding τ, the incorporation of a 2,2-dibromovinyl substituent in ACHV introduces unique electrostatic interactions that promote more ordered molecular packing, leading to an extended τ of 1.43 ns. By contrast, the τ of ACHM decreases slightly to 1.38 ns.[26]

The frontier molecular orbital energy levels of two SMAs were measured and calculated via cyclic voltammetry (CV), with the results shown in Figure 3h.[27] As expected, the modification of the molecular central unit with 2,2-dibromovinyl leads to a slight decrease in both the LUMO/HOMO energy levels of the acceptor molecules, with the experimental result showing excellent agreement with the DFT calculation results. Specifically, the LUMO/HOMO energy levels measured by CV are −3.85 eV/−5.69 eV for ACHM and −3.86 eV/−5.69 eV for ACHV, while the LUMO/HOMO energy levels obtained from DFT calculations are −3.49 eV/−5.54 eV for ACHM and −3.51 eV/−5.57 eV for ACHV (Figure S2).

To investigate the effect of introducing 2,2-dibromovinyl into the central unit of NFA on photovoltaic performance, we individually blended the two NFAs with the PM6, and OSCs were fabricated based on the conventional device structure: ITO/2PACz/PM6:acceptor/PNDIT-F3N/Ag.[28] The detailed optimization process is summarized in Tables S3−S5. The $J-V$ curves, external quantum efficiency (EQE) spectra, and comparison of photovoltaic parameters for the binary OSCs are shown in Figure 4a−c, respectively, with the relevant photovoltaic performance parameters summarized in Table 1. As indicated in Figure 4b, the devices based on PM6:ACHV exhibit a higher EQE response in the key absorption range of 500−815 nm, a characteristic that compensates for its lack of light absorption in the 895−920 nm range. Thus, although the EQE response range of the PM6:ACHV blend film is narrower than that of the PM6:ACHM blend film, the high EQE contribution in the key absorption range enables it to generate an J_{sc} that is nearly identical to that of the latter. On this regard, compared with OSC-based PM6:ACHM, OSC-based PM6:ACHV demonstrates a more favorable V_{oc} (0.908 V vs 0.886 V) and FF (75.40% vs 72.67%), ultimately delivering a PCE of 17.43%, higher than that of PM6:ACHM with a value of 16.38%.

To clarify the mechanism of 2,2-dibromovinyl on E_{loss} in OSCs, this study conducted a systematic analysis of the E_{loss} characteristics of the PM6:ACHM and PM6:ACHV systems, with detailed results summarized in Table S6. In OSCs, E_{loss} essentially refers to the dissipation of energy that is not effectively utilized during the conversion of photon energy to electrical energy. Based on the Shockley−Queisser (SQ) theory, it can be categorized into above-bandgap radiative recombination loss (ΔE_1), below-bandgap radiative recombination loss (ΔE_2), and nonradiative recombination loss (ΔE_3 or ΔE_{nr}), which satisfy the quantitative relationship: $E_{loss} = \Delta E_1 + \Delta E_2 + \Delta E_3$.[29,30] Among these, ΔE_1 represents the intrinsic radiative dissipation loss, while ΔE_2 denotes the sub-band gap radiative recombination loss. The E_g values of ACHM and ACHV are comparable, with values of 1.417 and 1.426 eV (Figure S7), respectively, which results in a minimal difference in ΔE_1 between the two. Specifically, the ΔE_1 values are 0.265 eV for ACHM and 0.266 eV for ACHV.[31] In terms of ΔE_2, ACHM exhibits a ΔE_2 of 0.067 eV, whereas ACHV has a slightly higher ΔE_2 (0.072 eV). It is speculated that this difference is associated with the variation in exciton dissociation driving force induced by the fine-tuning of acceptor energy levels.[32]

ΔE_3 refers to the energy loss arising from the dissipation of photogenerated carriers via nonradiative pathways, such as trap-state capture, molecular vibrational relaxation, and D/A interface recombination. It is the most dominant tunable energy loss component in the OSCs. The physical nature of ΔE_3 lies in the fact that carriers return to the ground state not through photon emission but by transferring energy to lattice vibrations (in the form of phonons) or being trapped by defect states, ultimately leading to irreversible energy dissipation that cannot be converted into usable electrical energy.

Two different methods were employed to calculate ΔE_3 in this study: one was derived from the energy loss decomposition formula $\Delta E_3 = q(V_{oc}^{rad} - V_{oc})$ and the other was quantified via the electroluminescence external quantum efficiency (EQE_{EL}) using the formula $\Delta E_3 = -k\mathrm{T}\ln(EQE_{EL})$.[33] For the PM6:ACHM system, the calculated and measured ΔE_3 values were 0.199 and 0.240 eV, respectively, while those for the PM6:ACHV system were 0.180 and 0.204 eV. This result indicates that ΔE_3 of the system can be effectively reduced via 2,2-dibromovinyl modification. Recent studies have demonstrated that the photoluminescence quantum yield (PLQY) can be used to characterize the radiative recombination

https://doi.org/10.1021/acs.joc.5c02377
J. Org. Chem. 2026, 91, 994−1003

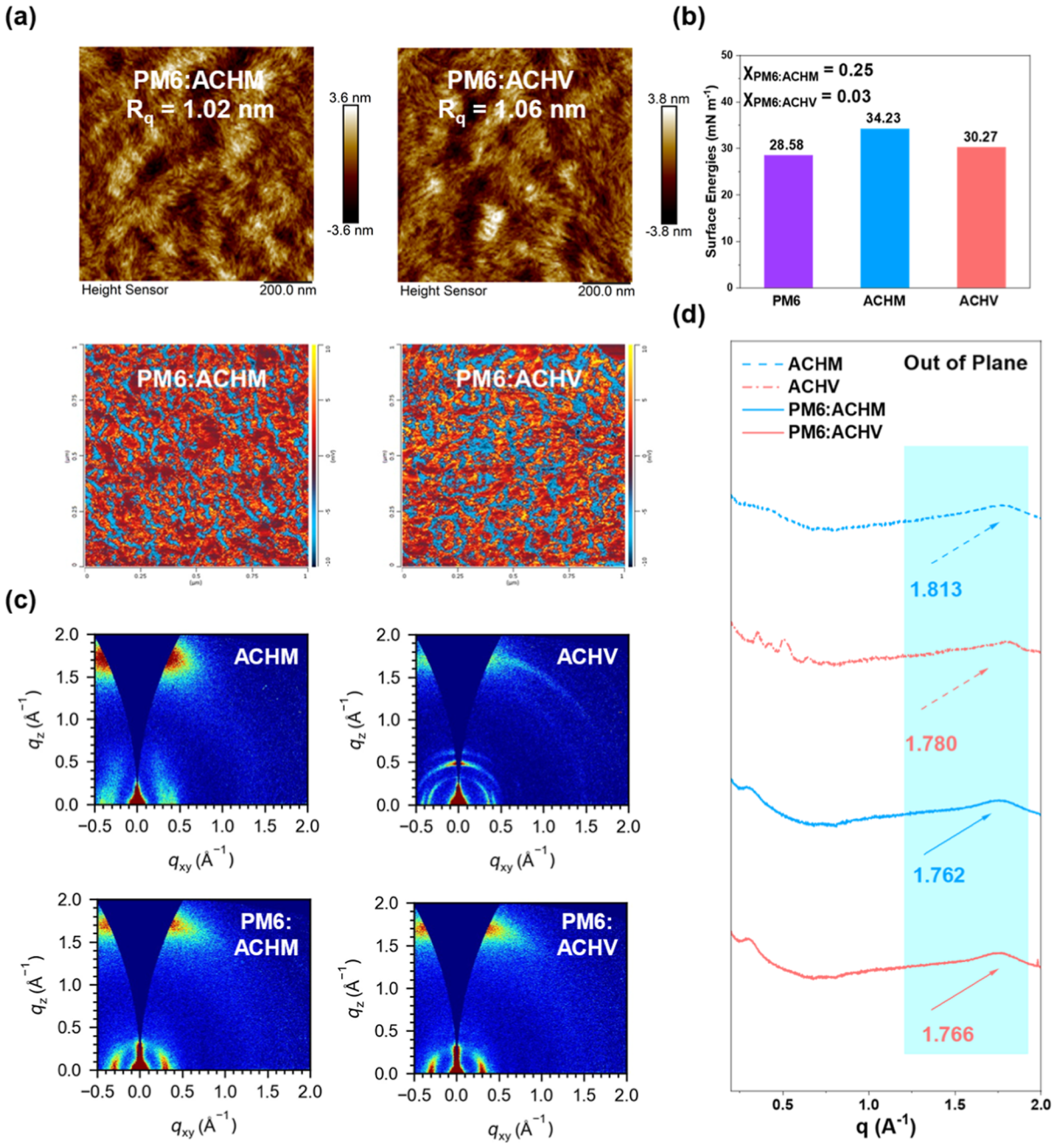

Figure 5. (a) AFM height images and AFM-IR images of two blended films. (b) Summary of the surface energy of PM6, ACHM, and ACHV, as well as their Flory−Huggins interaction parameters with PM6. (c) 2D GIWAXS patterns of ACHM and ACHV neat film and blended films. (d) Line-cut profiles of 2D In GIWAXS patterns ACHM and ACHV neat film and blended films.

efficiency of materials: a higher PLQY implies a lower proportion of nonradiative recombination and thus a smaller corresponding ΔE_3.[34] For NFAs, excessive molecular aggregation tends to induce an aggregation-caused quenching (ACQ) effect. This effect leads to a decrease in PLQY and a subsequent increase in ΔE_3. However, by introduction of 2,2-dibromovinyl into the central unit of the NFAs, its steric hindrance effect can effectively suppress the ACQ effect. Notably, the distinct packing modes of ACHM and ACHV directly influence this process; ACHM adopts three compact packing modes, which intensify intermolecular $\pi-\pi$ interactions, trigger ACQ, and elevate ΔE_{nr} to 0.199 eV, thereby limiting the V_{oc}. In contrast, ACHV forms two steric-modulated packing modes with moderate looseness, which inherently suppress ACQ. Consequently, the PLQY of ACHV is significantly increased to 6.46% (compared with 5.33% for ACHM), accompanied by a reduction in ΔE_3. Therefore, the higher V_{oc} can be attributed to the reduced energy loss.

To investigate the optimization mechanism of active layer morphology via introducing 2,2-dibromovinyl into the central unit, this study employed atomic force microscopy (AFM) and grazing-incidence wide-angle X-ray scattering (GIWAXS) to characterize the surface morphology and bulk packing structure. AFM image showed that the blend films of PM6:ACHM and PM6:ACHV exhibited relatively smooth surfaces, with root-mean-square (RMS) roughness of 1.02 and 1.06 nm, respectively. However, the AFM-IR image of the PM6:ACHM film clearly reveals pronounced aggregation of

https://doi.org/10.1021/acs.joc.5c02377
J. Org. Chem. 2026, 91, 994−1003

the ACHM acceptor, whereas the PM6:ACHV film presents uniformly distributed domains with appropriate sizes. Surface-energy measurements further elucidate the origin of this difference. As shown in Figure 5b, the Flory−Huggins interaction parameter (χ) between PM6 and ACHV is only 0.03, significantly lower than the value of 0.25 for PM6 and ACHM. This indicates stronger intermolecular interactions and better thermodynamic miscibility in the PM6:ACHV blend, enabling homogeneous mixing at the molecular level and effectively suppressing the spontaneous aggregation of ACHV. In contrast, the higher χ value of the PM6:ACHM blend reflects poorer compatibility, leading to a thermodynamic tendency toward phase separation. The face-on configuration of the donor and acceptor with strong $\pi-\pi$ stacking is critical for efficient vertical charge transport.

In the 2D GIWAXS patterns of neat acceptor films (see Figure 5c), both ACHM and ACHV neat films displayed distinct diffraction halos in the q_z direction (out-of-plane direction, OOP), confirming their ordered bulk packing and facilitating vertical charge transport.[35] Figure 5d and Table S7 indicate that the d-spacing of neat ACHM (3.47 Å) was significantly smaller than that of neat ACHV (3.53 Å), attributed to the moderately loose single-crystal packing of ACHV induced by the steric hindrance of 2,2-dibromovinyl. This steric effect did not disrupt ordered packing but led to ordered multiphase crystallization of ACHV in the OOP direction, corresponding to multiple diffraction rings in the q_z direction. In contrast, ACHM lacked such steric regulation, resulting in excessively strong intermolecular $\pi-\pi$ interactions and dense packing. Blending with PM6, the regulation of d-spacing differed between the two systems: PM6 alleviated the excessive aggregation of ACHM via moderate interactions with its conjugated backbone, reducing ACHM's packing density and increasing its d-spacing from 3.47 to 3.57 Å. For ACHV, which already had loose packing (d = 3.53 Å) due to steric hindrance, PM6 fine-tuned its packing state via intermolecular forces to make it slightly denser, leading to a slight decrease in d-spacing to 3.56 Å. This optimized d-spacing not only ensured sufficient intermolecular $\pi-\pi$ interaction strength for high charge mobility but also avoided charge transport channel blockage or charge recombination.[36]

Space-charge-limited current (SCLC) measurements characterized the electron (μ_e) and hole (μ_h) mobilities of blend films (Figure S11a). Compared with the ACHM-based device (μ_e/μ_h = 5.67 × 10^{-4}/5.39 × 10^{-4} cm^2 V^{-1} s^{-1}), the ACHV-based device showed increases in μ_e and μ_h to 5.77 × 10^{-4}/5.53 × 10^{-4} cm^2 V^{-1} s^{-1}, with the charge balance factor (μ_e/μ_h) slightly decreasing from 1.05 to 1.04. DFT calculations revealed that while ACHV's dipole moment decreased from 3.82 D (ACHM) to 2.97 D, which slightly weakened intramolecular charge separation. But its polarizability significantly rose from 1249 to 1340 au; this enhancement boosts electron cloud deformability and delocalization, accelerating exciton dissociation, thereby supporting efficient charge transport. Further, photocurrent density (J)-effective voltage (V_{eff}) measurements assessed exciton dissociation probability (P_{diss}) and charge collection efficiency (P_{coll}) (Figure S11b). The ACHV-based device achieved a P_{diss}/P_{coll} of 97.48%/84.25%, outperforming the ACHM-based device (96.82%/84.23%) and verifying the positive effects of electronic structure on charge separation.

Recombination dynamics upon 2,2-dibromovinyl incorporation was probed by light-intensity-dependent V_{oc} and J_{sc} measurements (Figure S11c,d). Corresponding $S/(kT/q)$ and α values were 1.18/0.989 (ACHM) and 1.39/0.997 (ACHV). The slight rise in $S/(kT/q)$ suggests steric-induced multiphase crystallization introduces minor local defects, moderately enhancing trap-assisted recombination. However, diversified ordered orientations markedly reduce carrier trapping and aggregation during transport, bringing α closer to the ideal value of 1, indicating enhanced carrier collection and suppressed transport-stage recombination losses, optimizing overall charge separation and transport efficiencies. Collectively, synergistic electronic structure and packing morphology optimization enable the ACHV-based device to achieve substantial V_{oc} enhancement while preserving a high FF.

3. CONCLUSION

This study further advanced the asymmetric modification strategy for the central unit of NFAs previously developed by our group and established an efficient synthetic method enabling the rapid asymmetric modification of 2,2-dibromovinyl at the central quinoxaline unit of NFAs, successfully preparing a novel acceptor named ACHV. Compared with the unmodified control acceptor ACHM, the incorporation of 2,2-dibromovinyl simultaneously enhanced the V_{oc} and FF without sacrificing the J_{sc}. OSCs based on ACHV achieved a PCE of 17.43%, with a V_{oc} of 0.908 V, J_{sc} of 25.57 mA·cm^{-2}, and FF of 75.40%. Notably, the E_{loss} of the ACHV-based device was as low as 0.518 eV, primarily attributed to the low ΔE_{nr} of 0.180 eV. This work validates the effectiveness of 2,2-dibromovinyl as a novel asymmetric modification unit, enriches the structural diversity and performance regulation precision of the central-unit asymmetric modification strategy, and provides a highly promising molecular design strategy for the design of OSC active layer materials with low E_{loss} and high PCE.

■ ASSOCIATED CONTENT

Data Availability Statement

The data underlying this study are available in the published article and its Supporting Information.

Supporting Information

The Supporting Information is available free of charge at https://pubs.acs.org/doi/10.1021/acs.joc.5c02377.

Experimental details, device fabrication, testing specifics, spectral data; and copies of ^{1}H, ^{13}C, and HMRS spectra (PDF)

Accession Codes

Deposition Number 2490039 contains the supplementary crystallographic data for this paper. These data can be obtained free of charge via the joint Cambridge Crystallographic Data Centre (CCDC) and Fachinformationszentrum Karlsruhe Access Structures service.

■ AUTHOR INFORMATION

Corresponding Authors

Xiangjian Wan − *State Key Laboratory of Elemento-Organic Chemistry, Frontiers Science Center for New Organic Matter, Key Laboratory of Functional Polymer Materials, Institute of Polymer Chemistry, Nankai University, Tianjin 300071, China;* orcid.org/0000-0001-5266-8510; Email: xjwan@nankai.edu.cn

https://doi.org/10.1021/acs.joc.5c02377
J. Org. Chem. 2026, 91, 994−1003

Yongsheng Chen − *State Key Laboratory of Elemento-Organic Chemistry, Frontiers Science Center for New Organic Matter, Key Laboratory of Functional Polymer Materials, Institute of Polymer Chemistry, Nankai University, Tianjin 300071, China;* orcid.org/0000-0003-1448-8177; Email: yschen99@nankai.edu.cn.

Authors

Jie Wang − *State Key Laboratory of Elemento-Organic Chemistry, Frontiers Science Center for New Organic Matter, Key Laboratory of Functional Polymer Materials, Institute of Polymer Chemistry, Nankai University, Tianjin 300071, China*

Jingyi Huo − *State Key Laboratory of Elemento-Organic Chemistry, Frontiers Science Center for New Organic Matter, Key Laboratory of Functional Polymer Materials, Institute of Polymer Chemistry, Nankai University, Tianjin 300071, China*

Xin Chen − *State Key Laboratory of Elemento-Organic Chemistry, Frontiers Science Center for New Organic Matter, Key Laboratory of Functional Polymer Materials, Institute of Polymer Chemistry, Nankai University, Tianjin 300071, China*

Jinyi Yang − *State Key Laboratory of Elemento-Organic Chemistry, Frontiers Science Center for New Organic Matter, Key Laboratory of Functional Polymer Materials, Institute of Polymer Chemistry, Nankai University, Tianjin 300071, China*

Longyu Li − *State Key Laboratory of Elemento-Organic Chemistry, Frontiers Science Center for New Organic Matter, Key Laboratory of Functional Polymer Materials, Institute of Polymer Chemistry, Nankai University, Tianjin 300071, China*

Ruibin Bian − *State Key Laboratory of Elemento-Organic Chemistry, Frontiers Science Center for New Organic Matter, Key Laboratory of Functional Polymer Materials, Institute of Polymer Chemistry, Nankai University, Tianjin 300071, China*

Wendi Shi − *State Key Laboratory of Elemento-Organic Chemistry, Frontiers Science Center for New Organic Matter, Key Laboratory of Functional Polymer Materials, Institute of Polymer Chemistry, Nankai University, Tianjin 300071, China*

Zhaoyang Yao − *State Key Laboratory of Elemento-Organic Chemistry, Frontiers Science Center for New Organic Matter, Key Laboratory of Functional Polymer Materials, Institute of Polymer Chemistry, Nankai University, Tianjin 300071, China;* orcid.org/0000-0003-1384-183X

Chenxi Li − *State Key Laboratory of Elemento-Organic Chemistry, Frontiers Science Center for New Organic Matter, Key Laboratory of Functional Polymer Materials, Institute of Polymer Chemistry, Nankai University, Tianjin 300071, China*

Complete contact information is available at: https://pubs.acs.org/10.1021/acs.joc.5c02377

Notes

The authors declare no competing financial interest.

■ ACKNOWLEDGMENTS

The authors gratefully acknowledge the financial support from the Ministry of Science and Technology of China (2022YFB4200400) and National Natural Science Foundation (52025033, 52373189, 22361132530).

■ REFERENCES

(1) Lin, Y.; Wang, J.; Zhang, Z. G.; Bai, H.; Li, Y.; Zhu, D.; Zhan, X. An Electron Acceptor Challenging Fullerenes for Efficient Polymer Solar Cells. *Adv. Mater.* **2015**, *27*, 1170.

(2) Yuan, J.; Zhang, Y.; Zhou, L.; Zhang, G.; Yip, H.-L.; Lau, T.-K.; Lu, X.; Zhu, C.; Peng, H.; Johnson, P. A.; Leclerc, M.; Cao, Y.; Ulanski, J.; Li, Y.; Zou, Y. Single-Junction Organic Solar Cell with over 15% Efficiency Using Fused-Ring Acceptor with Electron-Deficient Core. *Joule* **2019**, *3*, 1140−1149.

(3) Cui, Y.; Yao, H.; Zhang, J.; Xian, K.; Zhang, T.; Hong, L.; Wang, Y.; Xu, Y.; Ma, K.; An, C.; He, C.; Wei, Z.; Gao, F.; Hou, J. Single-Junction Organic Photovoltaic Cells with Approaching 18% Efficiency. *Adv. Mater.* **2020**, *32*, 1908205.

(4) Li, C.; Zhou, J.; Song, J.; Xu, J.; Zhang, H.; Zhang, X.; Guo, J.; Zhu, L.; Wei, D.; Han, G.; Min, J.; Zhang, Y.; Xie, Z.; Yi, Y.; Yan, H.; Gao, F.; Liu, F.; Sun, Y. Non-Fullerene Acceptors with Branched Side Chains and Improved Molecular Packing to Exceed 18% Efficiency in Organic Solar Cells. *Nat. Energy* **2021**, *6*, 605−613.

(5) Xue, Y.-J.; Lai, Z.-Y.; Lu, H.-C.; Hong, J.-C.; Tsai, C.-L.; Huang, C.-L.; Huang, K.-H.; Lu, C.-F.; Lai, Y.-Y.; Hsu, C.-S.; Lin, J.-M.; Chang, J.-W.; Chien, S.-Y.; Lee, G.-H.; Jeng, U. S.; Cheng, Y.-J. Unraveling the Structure-Property-Performance Relationships of Fused-Ring Nonfullerene Acceptors: Toward a C-Shaped ortho-Benzodipyrrole-Based Acceptor for Highly Efficient Organic Photovoltaics. *J. Am. Chem. Soc.* **2024**, *146*, 833.

(6) Wei, N.; Guo, Y.; Song, H.; Liu, Y.; Lu, H.; Bo, Z. Reducing Non-Radiative Energy Losses in Non-Fullerene Organic Solar Cells. *ChemSusChem* **2024**, *18*, No. e202402169.

(7) Zhu, L.; Zhang, J.; Guo, Y.; Yang, C.; Yi, Y.; Wei, Z. Small Exciton Binding Energies Enabling Direct Charge Photogeneration Towards Low-Driving-Force Organic Solar Cells. *Angew. Chem., Int. Ed.* **2021**, *60*, 15348.

(8) Zhao, Z.; Zhao, J.; Chung, S.; Cho, K.; Xu, W.; Kan, Z. Suppressing Bimolecular Charge Recombination and Energetic Disorder with Planar Heterojunction Active Layer Enables 18.1% Efficiency Binary Organic Solar Cells. *ACS Mater. Lett.* **2023**, *5*, 1718.

(9) Cui, Y.; Zhu, P.; Hu, H.; Xia, X.; Lu, X.; Yu, S.; Tempeld, H.; Eichel, R. A.; Liao, X.; Chen, Y. Impact of Electrostatic Interaction on Non-radiative Recombination Energy Losses in Organic Solar Cells Based on Asymmetric Acceptors. *Angew. Chem., Int. Ed.* **2023**, *62*, No. e202304931.

(10) Li, M.; Zhou, Y.; Zhang, J.; Song, J.; Bo, Z. Tuning the dipole moments of nonfullerene acceptors with an asymmetric terminal strategy for highly efficient organic solar cells. *J. Mater. Chem. A* **2019**, *7* (15), 8889−8896.

(11) Yang, Q.; Wu, R.; Yang, L.; Liu, W.; Meng, X.; Zhang, W.; Shen, S.; Li, M.; Zhou, Y.; Song, J. Tetrathiophene-based fully non-fused ring electron acceptors via asymmetric side chain engineering. *Dyes Pigm.* **2024**, *221*, 111808.

(12) Song, J.; Bo, Z. Asymmetric molecular engineering in recent nonfullerene acceptors for efficient organic solar cells. *Chin. Chem. Lett.* **2023**, *34* (10), 108163.

(13) Wu, R.; Meng, X.; Yang, Q.; Zhang, W.; Shen, S.; Yang, L.; Li, M.; Chen, Y.; Zhou, Y.; Song, J. Synergistically Regulating the Conjugation Length and Side Chain on Oligothiophene-Based Fully Nonfused Ring Electron Acceptors for Efficient Organic Solar Cells. *ACS Appl. Polym. Mater.* **2024**, *6* (23), 14668−14675.

(14) An, N.; Cai, Y.; Wu, H.; Tang, A.; Zhang, K.; Hao, X.; Ma, Z.; Guo, Q.; Ryu, H. S.; Woo, H. Y.; Sun, Y.; Zhou, E. Solution-Processed Organic Solar Cells with High Open-Circuit Voltage of 1.3 V and Low Non-Radiative Voltage Loss of 0.16 V. *Adv. Mater.* **2020**, *32* (39), 2002122.

(15) Zhu, J.; Zeng, R.; Zhou, E.; Li, C.; Deng, J.; Du, M.; Guo, Q.; Ji, M.; Wang, Z.; Lin, Y.; Han, F.; Zhuang, J.; Tan, S.; Kan, L.; Zhu, L.; Zhang, M.; Liu, F. A Refined Bulk P−I−N Structure in All-Polymer

Solar Cells To Achieve 20.1% Efficiency and Improved Stability. *J. Am. Chem. Soc.* **2025**, *147* (28), 24491−24501.
(16) Wang, J.; Chen, H.; Xu, X.; Ma, Z.; Zhang, Z.; Li, C.; Yang, Y.; Wang, J.; Zhao, Y.; Zhang, M.; Wan, X.; Lu, Y.; Chen, Y. An Acceptor with an Asymmetric and Extended Conjugated Backbone for High-Efficiency Organic Solar Cells with Low Nonradiative Energy Loss. *J. Mater. Chem. A* **2022**, *10*, 16714.
(17) Si, X.; Shi, W.; Wang, R.; Zhao, W.; Suo, Z.; Fu, Z.; Long, G.; Hao, X.; Yao, Z.; Wan, X.; Li, C.; Chen, Y. Suppressing Non-Radiative Recombination and Tuning Morphology via Central Core Asymmetric Substitution for Efficient Organic Solar Cells. *Nano Energy* **2024**, *131*, 110204.
(18) Wang, J.; Chen, X.; Zhao, W.; Yang, J.; Long, G.; Yao, Z.; Li, C.; Wan, X.; Chen, Y. Impact of Symmetric vs Asymmetric Conjugated Extensions in Acceptors on the Photovoltaic Performance of Organic Solar Cells. *Nano Energy* **2025**, *140*, 111028.
(19) Liu, K.; Jiang, Y.; Liu, F.; Ran, G.; Wang, M.; Wang, W.; Zhang, W.; Wei, Z.; Hou, J.; Zhu, X. The Critical Isomerization Effect of Core Bromination on Nonfullerene Acceptors in Achieving High-Performance Organic Solar Cells with Low Energy Loss. *Adv. Mater.* **2024**, *37*, 2413376.
(20) Zhou, P.; Lin, B.; Chen, R.; An, Z.; Chen, X.; An, Q.; Chen, P. Effect of Extending the Conjugation of Dye Molecules on the Efficiency and Stability of Dye-Sensitized Solar Cells. *ACS Omega* **2021**, *6*, 30069.
(21) Chen, H.; Liang, H.; Guo, Z.; Zhu, Y.; Zhang, Z.; Li, Z.; Cao, X.; Wang, H.; Feng, W.; Zou, Y.; Meng, L.; Xu, X.; Kan, B.; Li, C.; Yao, Z.; Wan, X.; Ma, Z.; Chen, Y. Central Unit Fluorination of Non-Fullerene Acceptors Enables Highly Efficient Organic Solar Cells with Over 18% Efficiency. *Angew. Chem., Int. Ed.* **2022**, *61*, No. e202209580.
(22) Qiu, D.; Xiong, S.; Lai, H.; Wang, Y.; Li, H.; Lai, X.; Zhu, Y.; He, F. Trifluoromethylation Enables Compact 2D Linear Stacking and Improves the Efficiency and Stability of Q-PHJ Organic Solar Cells. *Small* **2024**, *20*, 2403821.
(23) Badgujar, S.; Lee, G. Y.; Park, T.; Song, C. E.; Park, S.; Oh, S.; Shin, W. S.; Moon, S. J.; Lee, J. C.; Lee, S. K. High-Performance Small Molecule via Tailoring Intermolecular Interactions and its Application in Large-Area Organic Photovoltaic Modules. *Adv. Energy Mater.* **2016**, *6*, 1600228.
(24) Dai, T.; Meng, Y.; Wang, Z.; Lu, J.; Zheng, Z.; Du, M.; Guo, Q.; Zhou, E. Modulation of Molecular Quadrupole Moments by Phenyl Side-Chain Fluorination for High-Voltage and High-Performance Organic Solar Cells. *J. Am. Chem. Soc.* **2025**, *147*, 4631.
(25) Shi, Y.; Chang, Y.; Lu, K.; Chen, Z.; Zhang, J.; Yan, Y.; Qiu, D.; Liu, Y.; Adil, M. A.; Ma, W.; Hao, X.; Zhu, L.; Wei, Z. Small Reorganization Energy Acceptors Enable Low Energy Losses in Non-Fullerene Organic Solar Cells. *Nat. Commun.* **2022**, *13*, 3256.
(26) Cao, X.; Wang, P.; Jia, X.; Zhao, W.; Chen, H.; Xiao, Z.; Li, J.; Bi, X.; Yao, Z.; Guo, Y.; Long, G.; Li, C.; Wan, X.; Chen, Y. Rebuilding Peripheral F, Cl, Br Footprints on Acceptors Enables Binary Organic Photovoltaic Efficiency Exceeding 19.7. *Angew. Chem., Int. Ed.* **2024**, *64*, No. e202417244.
(27) Sun, Q.; Wang, H.; Yang, C.; Li, Y. Synthesis and Electroluminescence of Novel Copolymers Containing Crown Ether Spacers. *J. Mater. Chem.* **2003**, *13*, 800.
(28) Guan, S.; Li, Y.; Xu, C.; Yin, N.; Xu, C.; Wang, C.; Wang, M.; Xu, Y.; Chen, Q.; Wang, D.; Zuo, L.; Chen, H. Self-Assembled Interlayer Enables High-Performance Organic Photovoltaics with Power Conversion Efficiency Exceeding 20%. *Adv. Mater.* **2024**, *36*, 2400342.
(29) Gruber, M.; Wagner, J.; Klein, K.; Hörmann, U.; Opitz, A.; Stutzmann, M.; Brütting, W. Thermodynamic Efficiency Limit of Molecular Donor-Acceptor Solar Cells and its Application to Diindenoperylene/C60-Based Planar Heterojunction Devices. *Adv. Energy Mater.* **2012**, *2*, 1100.
(30) Ramirez, I.; Causa, M.; Zhong, Y.; Banerji, N.; Riede, M. Key Tradeoffs Limiting the Performance of Organic Photovoltaics. *Adv. Energy Mater.* **2018**, *8*, 1703551.
(31) Liu, S.; Yuan, J.; Deng, W.; Luo, M.; Xie, Y.; Liang, Q.; Zou, Y.; He, Z.; Wu, H.; Cao, Y. High-Efficiency Organic Solar Cells with Low Non-Radiative Recombination Loss and Low Energetic Disorder. *Nat. Photonics* **2020**, *14*, 300.
(32) Gao, W.; Qi, F.; Peng, Z.; Lin, F. R.; Jiang, K.; Zhong, C.; Kaminsky, W.; Guan, Z.; Lee, C. S.; Marks, T. J.; Ade, H.; Jen, A. K. Achieving 19% Power Conversion Efficiency in Planar-Mixed Heterojunction Organic Solar Cells Using a Pseudosymmetric Electron Acceptor. *Adv. Mater.* **2022**, *34*, 2202089.
(33) Liu, Q.; Vandewal, K. Understanding and Suppressing Non-Radiative Recombination Losses in Non-Fullerene Organic Solar Cells. *Adv. Mater.* **2023**, *35*, 2302452.
(34) Chen, X.-K.; Qian, D.; Wang, Y.; Kirchartz, T.; Tress, W.; Yao, H.; Yuan, J.; Hülsbeck, M.; Zhang, M.; Zou, Y.; Sun, Y.; Li, Y.; Hou, J.; Inganäs, O.; Coropceanu, V.; Bredas, J.-L.; Gao, F. A Unified Description of Non-Radiative Voltage Losses in Organic Solar Cells. *Nat. Energy* **2021**, *6*, 799.
(35) He, C.; Li, Y.; Liu, Y.; Li, Y.; Zhou, G.; Li, S.; Zhu, H.; Lu, X.; Zhang, F.; Li, C.-Z.; Chen, H. Near Infrared Electron Acceptors with a Photoresponse Beyond 1000 nm for Highly Efficient Organic Solar Cells. *J. Mater. Chem. A* **2020**, *8*, 18154.
(36) Hu, H.; Jiang, K.; Chow, P. C. Y.; Ye, L.; Zhang, G.; Li, Z.; Carpenter, J. H.; Ade, H.; Yan, H. Influence of Donor Polymer on the Molecular Ordering of Small Molecular Acceptors in Nonfullerene Polymer Solar Cells. *Adv. Energy Mater.* **2017**, *8*, 1701674.

https://doi.org/10.1021/acs.joc.5c02377
J. Org. Chem. 2026, 91, 994−1003